Preprint of R.Malki et al. Applied Mathematical Modelling 37 (2013) 3006–3020 http://dx.doi.org/10.1016/j.apm.2012.07.025

A Coupled Blade Element Momentum - Computational Fluid Dynamics Model for Evaluating Tidal Stream Turbine Performance

R. Malki, A. J. Williams, T. N. Croft, C. R. Bennett, M. Togneri and I. Masters

Marine Energy Research Group
College of Engineering, Swansea University, Singleton Park, Swansea, SA2 8PP, UK
r.malki@swansea.ac.uk, alison.j.williams@swansea.ac.uk, i.masters@swansea.ac.uk

Abstract A modelling approach based on Blade Element Momentum Theory is developed for the prediction of tidal stream turbine performance in the ocean environment. Through the coupling of the Blade Element Momentum method with Computational Fluid Dynamics, the influence of upstream hydrodynamics on rotor performance is accounted for. Incoming flow onto the rotor can vary in speed and direction compared to free-stream conditions due to the presence of obstructions to the flow in the upstream, due to other devices for example, or due to the complexity of natural bathymetries. The relative simplicity of the model leads to short run times and a lower demand on computational resources making it a useful tool for considering more complex engineering problems consisting of multiple tidal stream turbines. Results from the model compare well against both measured data from flume experiments and results obtained using the Classical Blade Element Momentum model. A discussion considering the advantages and disadvantages of these different approaches is included.

Keywords: blade element momentum theory, computational fluid dynamics, tidal stream turbines

1 Introduction

The exploitation of tidal streams for energy generation offers a viable route to decreasing Britain's dependence on fossil fuels. The most suitable offshore locations are dominated by high velocity and highly turbulent flows. The installation of tidal stream turbines and their operation in such complex environments can be potentially very difficult [1]. Minimising risks taken by developers and stakeholders can only be achieved by a better understanding of these environments and how such devices are likely to perform within them. This can be achieved through laboratory models, scaled or full-scale offshore deployments or through numerical simulation. A key advantage of numerical simulation is the lower risk and cost, although there is clearly a need for validation against measured data. Numerical models are also useful for predicting environmental impacts of tidal stream turbines [2]. Although laboratory models cannot truly mimic complex offshore conditions, they are very convenient due to significantly lower costs compared to offshore deployments, and for the possibility to collect accurate and repeatable data.

The explicit modelling of turbine blades can be achieved through computational fluid dynamics [3], although this can be quite demanding on computational resources. An alternative approach is the classical Blade Element Momentum (BEM) method, which was developed by Glauert [4] and has been used for the analysis of propellers, particularly within the helicopter industry [5], and more recently, wind turbines [6] using tabulated airfoil data. The simplicity of the model and the agreement of its results with measured data have helped to make it the most popular design tool for analysing the aerodynamic loading on wind turbine rotors with no feasible alternatives. The BEM method has also been applied successfully to tidal turbines [7]. The method requires the discretisation of the rotor into typically 10-20 annuli [8] and it is assumed that each annulus can be treated independently. A stream tube can therefore be extended through each annulus to both the far upstream and far downstream. However, due to the complexity of flow situations encountered by a typical rotor, various empirical corrections have been introduced for unsteady flows, yawed rotors [9,10], hub losses [11], tip losses [4,12] and heavily loaded rotors [9,13]. Masters et al. [7] implement many of these in a tidal context.

One of the key limitations of the BEM method is that it cannot be used for analysing the influence of a rotor on the surrounding flow. Where an analysis of wake dynamics is required, alternative modelling approaches must be employed. A number of such alternatives have been developed for evaluating wind turbine wakes, although they have not been widely adopted at an industrial level due to high computational resource requirements. Comprehensive reviews have been presented on these models [14-20]. The BEM model remains the industry's preferred design tool.

Despite the similarities between tidal and wind turbines, and although extensive work has been performed on the latter, there has been significantly less focus on tidal power. Yet there is much that can be learned from the accumulated knowledgebase associated with the wind power industry. This comes at a vital time when numerous tidal power trial schemes have been granted consent and planning is likely to commence in the near future for larger array deployments. There is therefore a clear need for practically useable tools to aid in the planning and implementation of tidal power schemes, and to predict the performance of tidal turbines in offshore environments.

A Blade Element Momentum - Computational Fluid Dynamics (BEM-CFD) model is presented here and is based on the actuator disk approach [21], but accounts for variations in blade geometry and its hydrodynamic properties. In the BEM-CFD model, a turbine is represented by a permeable disc through which the flow is allowed to pass whilst being subjected to the influence of surface forces due to the blades. Blade representation is based on the BEM method within the solution of the conservation laws as characterised by the Euler or Navier-Stokes equations.

Linking the CFD flow domain to the BEM model is achieved by additional source terms included within the conservation of momentum equations of a typical finite volume computational fluid dynamics solver, in this case *PHYSICA* [22], which has been developed by Croft et al. [23]. By resolving the flow around the rotor, the interdependence of the annuli within the BEM model is accounted for, and the empirical corrections listed above are no longer required. The actuator disk implemented here is non-uniformly loaded with the force varying according to axial and radial position. Validation of the model is conducted against measured flume data collected by Bahaj et

al. [24] using a 0.8 m diameter turbine. To achieve this comparison, a blockage correction based on conservation of fluid mass through a streamtube passing through the rotoris implemented to the simulation results. The same methodology was implemented by Bahaj et al. [24] to produce the published flume data . The BEM-CFD is applied to an unconstrained CFD solution domain as a more direct approach to minimising blockage effects and the results are also compared to the more widely used classical BEM model which does not account for the local flow field around the rotor.

2 The BEM-CFD Model

2.1 The governing equations

The CFD model depends upon the solution of the Navier–Stokes equations which represent the conservation of mass and momentum. The steady-state equations for mass and momentum are expressed mathematically as:

$$\nabla.(\rho \underline{u}) = 0 \tag{1}$$

$$\nabla.(\rho \underline{u} u_i) = -\frac{\partial p}{\partial x_i} + \nabla.(\mu_{lam} + \mu_t)\nabla u_i + S_i \tag{2}$$

where ρ is the density, u_i is the i'th component of the velocity vector, μ_{lam} and μ_t are the dynamic laminar and turbulent viscosities respectively, and S_i includes any additional sources (for example the source due to the moving rotor).

The effect of turbulence is resolved through the k-ε model [25]. In this model two equations are solved, the first representing the energy contained with the turbulence, represented by the symbol *k*, and the second dissipation of this energy, represented by the symbol ε. The equations for the transport of these variables are similar in form to the momentum equations:

$$\nabla.(\rho \underline{u} k) = \nabla.\left(\mu_{lam} + \frac{\mu_t}{\sigma_k}\right)\nabla k + \mu_t G - \rho\varepsilon \tag{3}$$

$$\nabla.(\rho \underline{u} \varepsilon) = \nabla.\left(\mu_{lam} + \frac{\mu_t}{\sigma_\varepsilon}\right)\nabla \varepsilon + \frac{\varepsilon}{k}\left(C_{1\varepsilon}\mu_t G - C_{2\varepsilon}\rho\varepsilon\right) \tag{4}$$

These equations are used to calculate a turbulent viscosity:

$$\mu_t = \frac{\rho C_\mu k^2}{\varepsilon} \tag{5}$$

In equations (3), (4) and (5) σ_k, σ_ε, $C_{1\varepsilon}$, $C_{2\varepsilon}$ and C_μ are taken to be constants, and G represents the turbulent generation rate. The turbulent viscosity is added to the laminar viscosity and the sum is used as the viscosity in the diffusion terms in the momentum, k and ε equations.

2.2 Representation of Rotor - Blade Element Method

For the actuator disc method, the influence of a turbine with multiple blades is time-averaged over a significant time interval. The influence of the blades becomes evenly distributed over the area of influence of the turbine, and the rotor applies the same force to all locations at the same radial distance from the rotor centre on a given axial plane. Magnitudes of such forces are a function of blade geometry and its hydrodynamic properties as characterised by the variations in lift and drag coefficients with the angle of attack of the flow. The blade used here is based on the experiments presented in [24]. Lift and drag coefficient properties are presented in [26].

Source terms which are functions of radial and axial position are applied to each of the momentum equations that represent the force on the fluid due to the blades of the turbines. The advantage of this approach is that the physical characteristics of the blade are introduced through the source terms rather than being specifically resolved using an exact geometry allowing better quality meshes. The disadvantage is that because of the Reynolds averaged nature of the solution, it fails to resolve any transient flow features due to blade position.

Figure 1a shows the discretisation of a three-bladed turbine in the blade element method approach. The blade properties at a certain radius, r, are determined and are then averaged throughout the whole of the shaded region. This is repeated for each blade element over the radius of the rotor. In Figure 1b a close-up schematic of a blade element is shown indicating the chord length, c, the element thickness, t, and the radial width, dr.

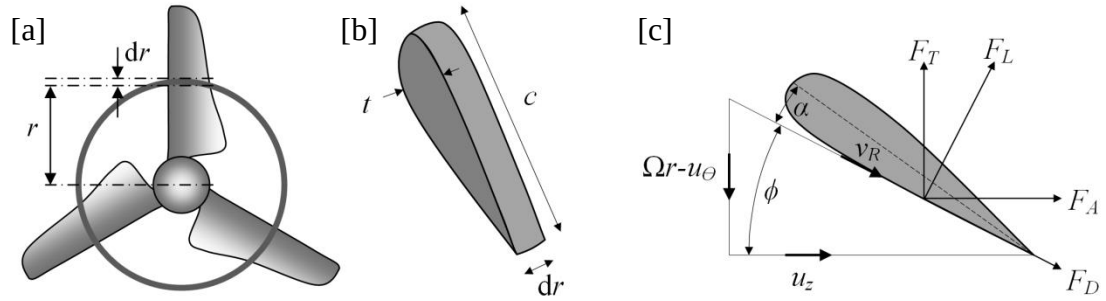

Figure 1 [a]: Schematic of discretisation of the rotor; [b]: Schematic of blade element; [c]: Resolution of lift and drag forces

Each element experiences forces due to the fluid. These consist of axial and tangential components as shown in Figure 1c. Here F_T is the torque and F_A represents the axial force. The lift, F_L, and drag, F_D, forces are dependent on the angle of attack, α, which occurs between the blade element and the resultant velocity, v_R (Figure 1c). Based on the approach in Griffiths [27], an axial force on a blade element can be defined as follows:

$$F_A = F_L \sin\phi + F_D \cos\phi \tag{6}$$

and the tangential force on a blade element, which is equal to the torque/radius, i.e. *dT/r*, can be defined as:

$$F_T = F_L \cos\phi - F_D \sin\phi \tag{7}$$

where ϕ is the flow inclination angle defined by:

$$\phi = \tan^{-1}\left(\frac{\Omega r - u_\theta}{u_z}\right) \tag{8}$$

Here u_θ and u_z are the tangential and axial velocities respectively, and Ω is the angular velocity in rad/s. The lift force, F_L, and drag force, F_D, are given as follows:

$$F_L = \frac{1}{2}\rho|v_R|^2 C_L c\mathrm{d}r \tag{9}$$

$$F_D = \frac{1}{2}\rho|v_R|^2 C_D c\mathrm{d}r \tag{10}$$

Here C_L and C_D are the lift and drag coefficients respectively, and

$$|v_R|^2 = u_z^2 + (\Omega r - u_\theta)^2 \tag{11}$$

Substituting (9) and (10) into (6) and (7) gives the following equations:

$$S_z = F_A = \frac{1}{2}\rho|v_R|^2 c\mathrm{d}r(C_L \sin\phi + C_D \cos\phi) \tag{12}$$

$$S_\theta = F_T = \frac{1}{2}\rho|v_R|^2 c\mathrm{d}r(C_L \cos\phi - C_D \sin\phi) \tag{13}$$

which, when resolved into Cartesian components and converted into a force per volume, are substituted into the momentum equations (2) through the source terms, S_i.

2.3 Computational solution procedure

The Navier-Stokes equations are solved within the CFD model to calculate velocity and pressure parameters throughout the flow domain. The solution is dependent on the initial and boundary conditions which are implemented to set up the model. Meanwhile, at the location of the blades, a source term is introduced using the BEM model which is dependent on the blade characteristics and the tip speed ratio. Throughout the simulation,

there is a closely coupled interaction between the CFD model and the BEM model at every iteration. The solution procedure is illustrated through the schematic diagram presented in Figure 2.

The solution to the set of governing equations (1)-(4) is achieved using a collocated cell centred finite volume method. The solution domain is split into a number of non-overlapping mesh elements (see Section 3.3). The governing equations are discretised using cell-centred approximations to the variables, where the control volume is the mesh element itself.

The continuity, momentum and turbulence equations can be written in the general form

$$\frac{\partial \rho\phi}{\partial t} = \nabla.\left(\Gamma_\phi \nabla\phi\right) + Q_v - \nabla.\left(\rho\phi\underline{u}\right)$$

where the values of the variables ϕ, Γ_ϕ and Q_v are defined as shown in Table 1.

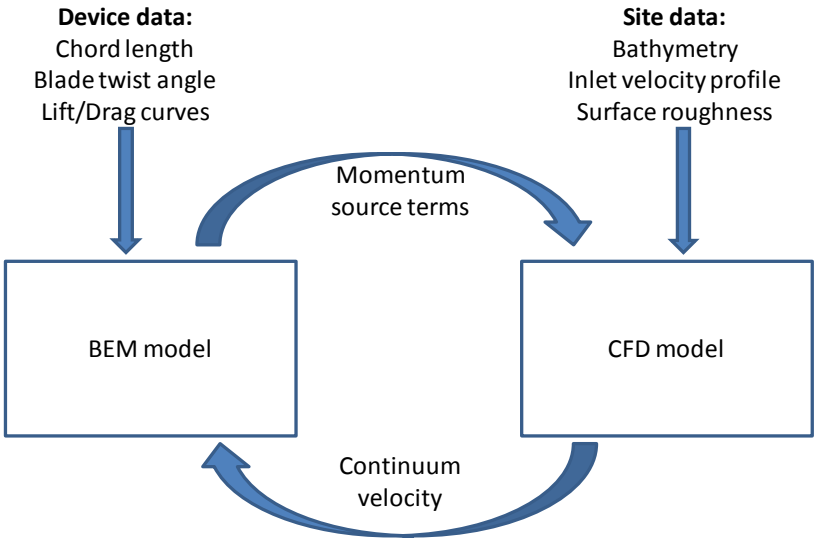

Figure 2 Schematic diagram of the solution procedure of the actuator disc model

Table 1 Definition of terms in the generic transport equation.

Phenomenon	ϕ	Γ_ϕ	Q_v
Continuity	1	0	0
Velocity	u_i	$\mu_{lam}+\mu_t$	$-\frac{\partial p}{\partial x_i}+S_i$
Turbulent energy	k	$\mu_{lam}+\frac{\mu_t}{\sigma_k}$	$\mu_t G-\rho\varepsilon$
Turbulent dissipation	ε	$\mu_{lam}+\frac{\mu_t}{\sigma_\varepsilon}$	$\frac{\varepsilon}{k}\left(C_{1\varepsilon}\mu_t G-C_{2\varepsilon}\rho\varepsilon\right)$

2.4 Definitions

The tip speed ratio (TSR), the ratio between the rotational speed of the tip of the blades and the free-stream horizontal velocity, is defined by

$$TSR = \frac{\Omega R}{U} \tag{14}$$

where U is the upstream free velocity.

The performance of a rotor can be characterised using the power coefficient, C_P, and thrust coefficient, C_F, which are expressed as follows

$$C_P = \frac{P}{\frac{1}{2}\rho U^3 A} = \frac{\int_0^R \Omega F_T}{\frac{1}{2}\rho U^3 A} \tag{15}$$

$$C_F = \frac{F_A}{\frac{1}{2}\rho U^2 A} = \frac{\int_0^R F_A}{\frac{1}{2}\rho U^2 A} \tag{16}$$

In the computational model the integrals in (15)-(16) are calculated from a summation over each element as calculated from (12)-(13).

3 Numerical Simulations and Validation Methods

3.1 Measured Tow-Tank Data

The simulations presented in this study are based on the tow-tank experiments conducted by Bahaj et al. [24] for a 0.8 m diameter, three-bladed turbine with hub pitch angles of 20 and 25 degrees. The authors consider a range of different conditions, as well as cavitation tunnel experiments.

The blade geometry as well as the lift and drag coefficient values required for characterising the source terms within the BEM-CFD model are provided in the experimental publication. The width, depth and length of the tow tank, are 3.7 m, 1.8 m and 60 m respectively, with the 0.8 m diameter rotor placed 3.59 m downstream of the inlet (see Figure 3a). An approximation to the nacelle from the tow tank experiments [24] is included in the mesh. The diameter of the horizontal main body is 0.1 m, and the total length from nose to tail of the nacelle is 1.0 m. In [24], it is stated that the downstream position of the upright support that connects the nacelle to the tow rig is chosen to have minimal effect on rotor performance. Therefore the upright support has not been included in the computational model. In Figure 3b, a view of the rotor disk in the y-z plane is

presented. The centre of the rotor is located at x = 0.03 m, y = z = 0 m. Two hub pitch angles were considered: 20° and 25°.

In the experimental study, the effect of depth of immersion on the rotor performance was investigated by varying the magnitude of 'H' shown in Figure 3. Two tip immersions were considered: 'shallow' (H = 0.15 m), and 'deep' (H = 0.44 m). The deep tip immersion condition is equivalent to a distance of approximately half a diameter from the water surface and is therefore very close to the water surface and surface effects are still likely to be significant. The tow tank domain is enclosed apart from the top where there is a free surface and the rotor is pulled along the length of the tank at a speed u_{exp} m/s which varied for different experiments are presented in Table 2.

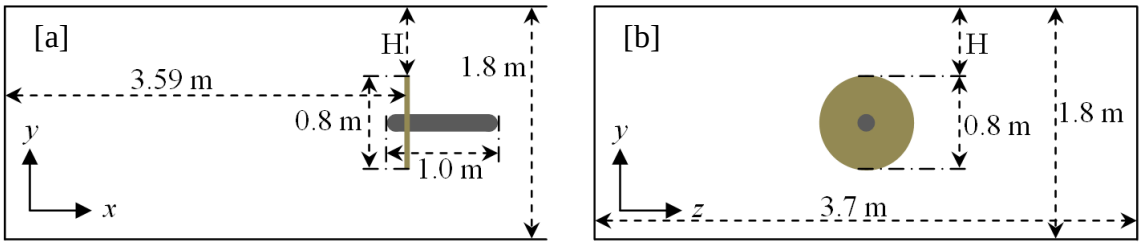

Figure 3 Schematic showing the position of rotor and nacelle a) in relation to the inlet boundary in the x-y plane and b) in the lateral z-y plane.

Table 2 Free stream velocity values for test cases

Hub pitch	20°		25°	
H (m)	0.15	0.44	0.15	0.44
u_{exp} (m/s)	1.5	1.5	1.2	1.4

3.2 Classical Blade Element Momentum Method

The principles of Blade Element Momentum Theory (BEMT) were explained earlier in Section 2.2 where the characterisation of the rotor within the model was discussed. In its classical form, it is commonly used to evaluate the performance of rotors as characterised by C_P values.

The BEM model used in this study to produce performance curves for the turbine blades used in [24] is presented in [7] where it is validated against *GH Tidal Bladed*, which is widely considered to be the industry standard. The model was applied whilst implementing the Glauert tip loss equation [4] and a hub loss model proposed by Moriarty and Hansen [11].

Axial and tangential induction factors (a and b respectively) are defined as follows:

$$a = \frac{u}{U} \tag{17}$$

$$b = \frac{\omega}{2\Omega} \tag{18}$$

where for any given stream tube passing through the rotor, u and U are the longitudinal velocities at the blade and in the free-stream respectively, whereas ω is the rotational velocity of the flow in the immediate wake and Ω is the rotational velocity of the blades. Values of the axial induction factor greater than 0.5 correspond to a physically unrealistic reversal of flow in the rotor wake; classical BEMT cannot, therefore, handle such values of a. We therefore introduce a high-induction correction, which uses a different, semi-empirical, relationship between disc thrust loading and the axial induction factor when a exceeds some specified critical value (typically around 0.4).

Strictly speaking, the axial and induction factors are used to characterise the flow properties at the location of the blade. These definitions are also useful for evaluating flow recovery downstream of the rotor, and for that purpose, the normalised longitudinal velocity and normalised area mean angular velocity (a' and $\bar{b}$) are synonymous with the definitions for a and b respectively, except they are applied away from the rotor. The value of $\bar{b}$ is determined by averaging over the area of influence of the rotor (0.8 m diameter) at any given longitudinal distance downstream.

3.3 BEM-CFD Simulations and Blockage Corrections

Simulations were conducted using the model outlined earlier in Section 2. The model domain was therefore based on the cross-sectional geometry of the tow-tank (Section 3.1) and the terms 'shallow tip immersion' and 'deep tip immersion' used by Bahaj et al. [24] in reference to 'H' values of 0.15 m and 0.44 m respectively are retained herein. To investigate the effect of immersion, the model domain is occupied completely by the flow and the rotor is positioned so that height H, shown in Figure 3, represents the tip immersion.

Since the experiments were conducted in a tow-tank, the influence of different flows on the performance of a device is evaluated by dragging it through the stationary water at the velocities listed in Table 2. However, for the numerical simulations, the rotor remains fixed in location as water flows past it. A constant plug flow is introduced at the inlet with magnitude u_{exp} (see Table 2), a symmetry boundary is implemented in place of the water surface and a zero-pressure boundary is implemented at the downstream end of the domain. The axial component of velocity on the side walls and bed of the domain are fixed to u_{exp} which is intended to simulate a wide and deep domain where wall effects are completely absent, particularly at the location of the rotor.

Naturally, laboratory investigations are often restricted by limitations, and in this case, the depth of the flume is only 2.25 times greater than the turbine diameter and hence, blockage effects are likely to be significant. Bahaj et al. [24] attempt to correct for these errors and the reader is advised to refer to their publication for further clarification on their correction approach. The following correction factor was applied by Bahaj et al. [24] and will be considered as one of the options for blockage correction of the results presented in this study:

$$\text{Correction Factor} = \left(\frac{U_T}{U_F}\right)^n = \left(\frac{4(U_1/U_T)}{4(U_1/U_T)^2+(U_2/U_T)^2([U_3/U_2]^2-1)}\right)^n \quad (19)$$

where U_T is the upstream velocity, U_1 is the velocity through the rotor, U_2 is the downstream in-wake velocity and U_3 is the downstream out-of-wake velocity. The correction factor is then applied to the tip speed ratio (n = 1), the thrust coefficient (n = 2) and the power coefficient (n = 3) to correct the respective curves of the performance parameters.

In setting up numerical models, this is one area where the user faces relatively fewer restrictions and therefore, we adopt a more direct method for minimising blockage errors and we consider a third domain geometry where the width and depth are both increased to: 4.80 m; 6.0 times greater than the turbine diameter. The turbine in this case is centred vertically within the water column resulting in an equivalent 'H' value of 2.0 m, and this will be referred to as the 'unconstrained' condition.

A relatively high mesh resolution is implemented at the location where the source terms characterising the rotor are implemented to capture spatial variations associated with blade properties in an adequate level of detail. This will be referred to as the 'blade region' (see Figure 4). A high mesh resolution, albeit to a lesser extent, is maintained in the vicinity of the rest of the turbine structure and in the region immediately downstream, where acceleration of the flow is significant. The mesh resolution is gradually reduced by increasing element size towards the outer edges of the model domain. Details of the mesh resolution across the domain are summarised in Figure 4 and Table 3.

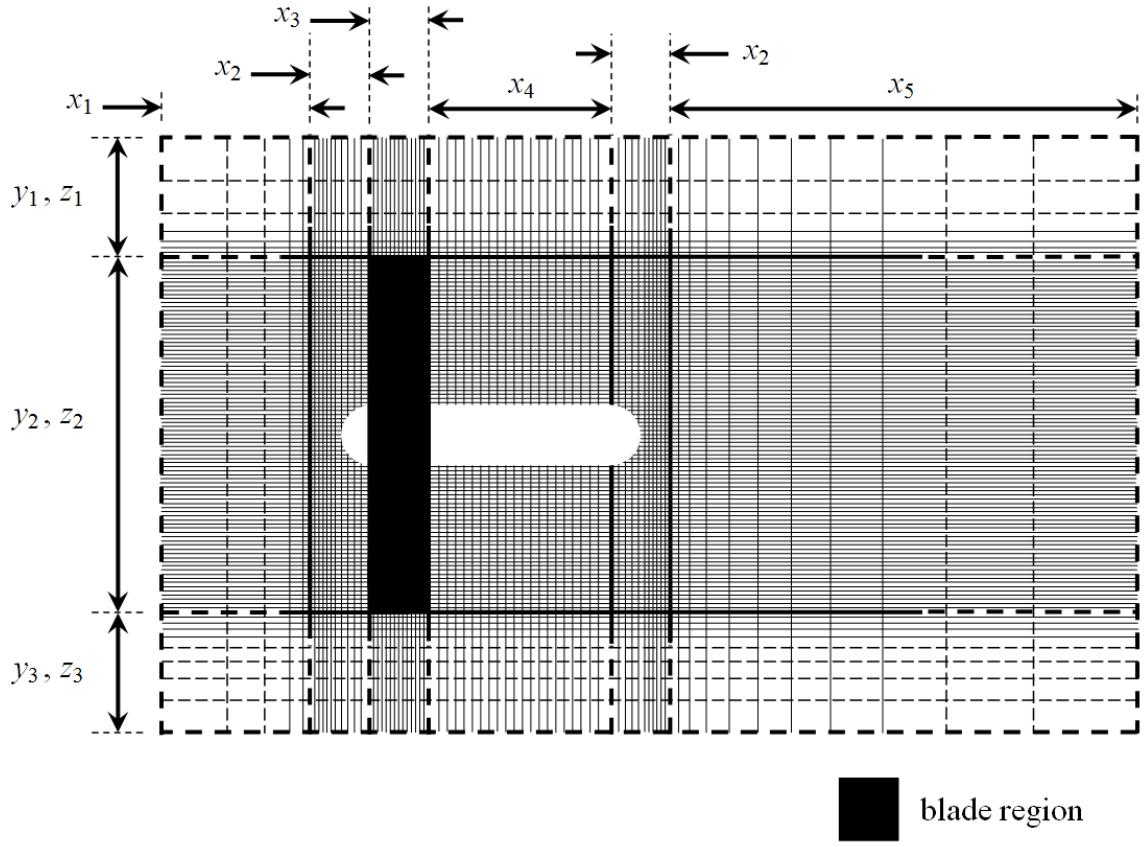

Figure 4 Schematic diagram illustrating mesh resolution across the model domain

Table 3 Mesh divisions along the lengths described in Figure 4

	Shallow tip		Deep tip		Unconstrained	
Section	Length	Divisions	Length	Divisions	Length	Divisions
x_1	3.45 m	40	3.45 m	40	3.45 m	40
x_2	0.15 m	24	0.15 m	24	0.15 m	24
x_3	0.06 m	20	0.06 m	20	0.06 m	20
x_4	0.74 m	40	0.74 m	40	0.74 m	40
x_5	50.00 m	80	50.00 m	80	50.00 m	80
y_1	0.00 m	0	0.28 m	6	1.85 m	10
y_2 , z_2	1.10 m	52	1.10 m	52	1.10 m	52
y_3	0.69 m	10	0.40 m	10	1.85 m	10
z_1 , z_3	1.29 m	10	1.29 m	10	1.85 m	10

4 Results and Discussion

To validate the BEM-CFD model a comparison is performed with the experimental tow-tank results published by Bahaj [24] which were summarised above. Power and thrust coefficient variations with the tip speed ratio were also determined using classical blade element momentum theory with hub and tip loss corrections [7] for further comparison with the results of the BEM-CFD model.

4.1 Convergence of Power Coefficients and Mesh Dependency of Solution

To evaluate convergence and mesh dependency of the solutions, simulations were conducted for a range of mesh densities within the blade region where the source terms are introduced and were run for 100,000 iterations each. This was performed using the unconstrained domain geometry outlined in Section 3.3. Variation in the power coefficient, C_P, is monitored to evaluate convergence. The blade region is 0.06 m in the flow direction (x) and 1.10 m in each of the vertical (y) and lateral (z) directions. Mesh resolutions considered in the blade region ranged between 5 and 40 elements in the flow direction (along x_3 in Figure 4), and between 26 and 78 elements in the lateral (z_2) and vertical (y_2) directions. Convergence of performance coefficients occurs at around 10,000 iterations (see Figure 5a).

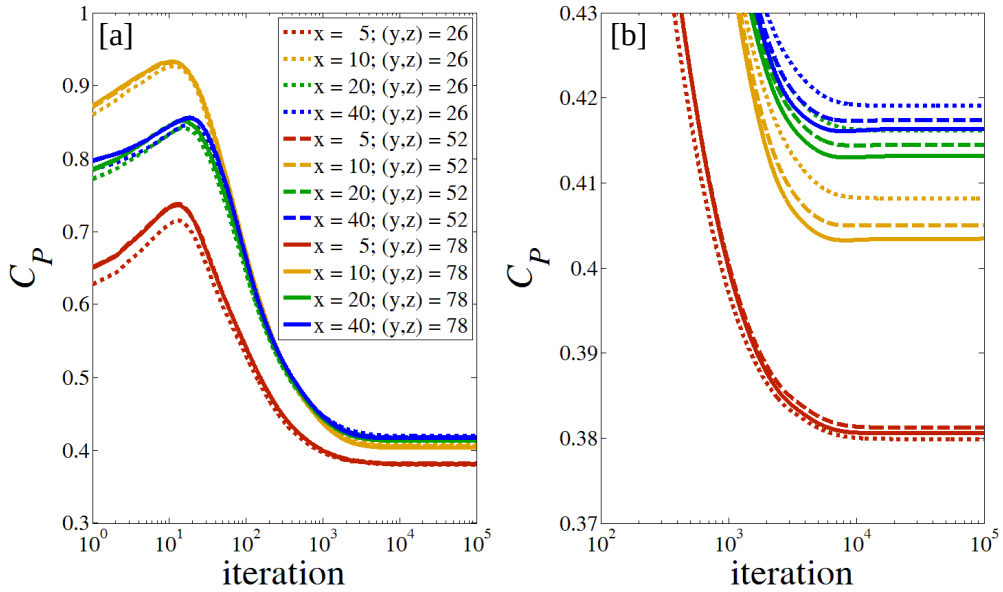

Figure 5 [a]: Convergence of the power coefficient, C_P, for different mesh resolutions within the blade region; [b]: a close-up of the curves near convergence

For the range of mesh resolutions considered, an increase in the number of elements along the *x* direction resulted in increasing C_P values whereas an increase in the *y* and *z* directions usually resulted in a decrease (see Figure 5b). Using the highest mesh resolution considered (x = 40; y = z = 78) as the most accurate indicator of the performance of the turbine, a C_P value of 0.416 was predicted for the rotor. C_P values increased with increasing mesh resolution within the blade region along the flow direction. With the exception of the lowest longitudinal mesh resolution (x = 5 elements), C_P values decreased with increasing mesh resolution along the lateral and vertical directions. Errors ranged between 0.3 % and 8.8 %. Mesh resolution used throughout this paper is 20 elements along the flow direction and 52 elements along the lateral and vertical directions which corresponds to an error in C_P of 0.4 % (a C_P value of 0.414 was predicted). Simulations conducted for this study are run for 13,000 iterations, by which point changes to values of the coefficients with further iterations are insignificant.

4.2 Comparison of Power and Thrust Coefficients

Simulations of the tow-tank experiments were conducted for a range of tip speed ratios (TSR) based on the available measured data. Comparisons of the variation in power (C_P) and thrust (C_F) coefficients with TSR determined through physical and numerical simulations for shallow (H=0.15 m) and deep (H=0.44 m) tip immersions are presented in Figure 6 and Figure 7 for hub pitch angles of 20° and 25° respectively. The experimental and BEM-CFD model both predict a peak performance occurring at a TSR value between 5.0 and 6.0. For larger TSR values, there is a sharp drop in performance. As the TSR increases for a given free-stream velocity, the angle of attack (Figure 1c) decreases and the lift and drag forces act almost perpendicular and parallel to the blade respectively, hence, more of the flow is diverted away from the blade and the blade becomes less efficient.

The experimental results indicate a clear improvement in performance with increasing submergence level of the turbine as shown by an increase in both power and thrust coefficients. These trends are discussed in some detail by Bahaj et al. [24], and are ultimately linked to free-surface effects. For a shallow tip immersion, the turbine is closer to the free surface which limits expansion of the wake and hence, a smaller pressure difference occurs across the turbine.

For the BEM-CFD simulation, a symmetry wall boundary condition was implemented in place of the free water surface which requires that there is no flow or scalar flux across the boundary [28]. Variations in water surface elevation are not captured and hence, errors are likely to be large where free surface effects are significant as demonstrated by Consul et al. [29]. There was no difference between the power and thrust curves for the two submergence conditions indicating that where free surface conditions are significant, an alternative approach is required for modelling the water surface. The authors' work on filling mould cavities using a volume of fluid approach for the free surface [30] has shown this to be a significant computational overhead.

As discussed earlier, the power and thrust curves taken from Bahaj et al. [24] have been corrected for blockage effects. Due to the confined cross-sectional area of the tow-tank in which the experiments were conducted, a larger proportion of the flow is likely to be forced through the turbine, rather than moving around the device due to a more usual expansion of the flow around an obstruction. This concept may give rise to a better performance than would otherwise be expected. The BEM-CFD results at this stage have not been corrected for blockage effects, although this will be addressed at a later stage (see Section 4.3). However, this explains the greater magnitude of coefficient values when compared to the experimental results. The trends observed are virtually identical for the two hub pitch angles.

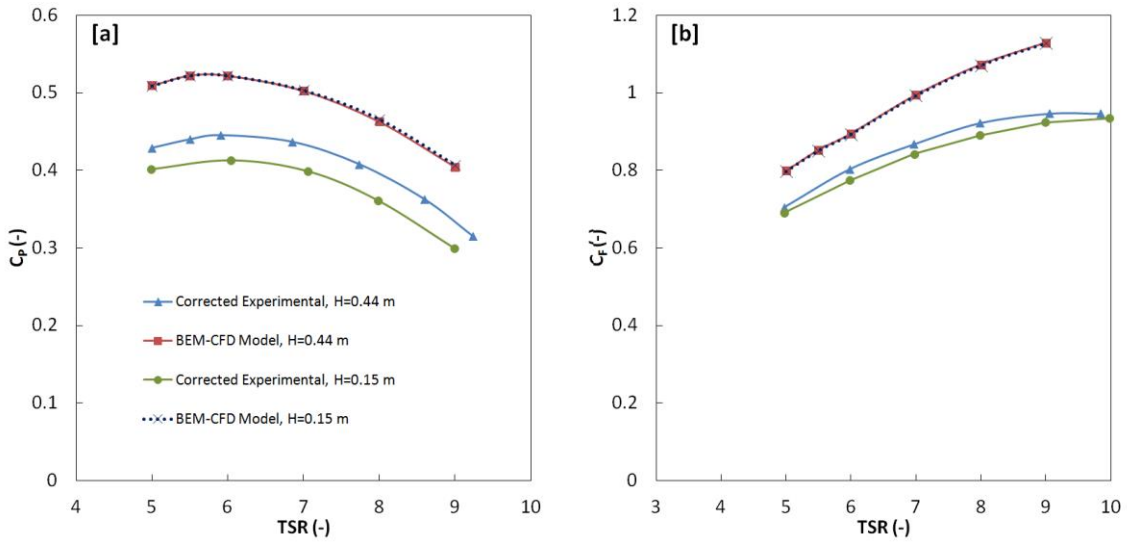

Figure 6 A comparison of experimental and BEM-CFD model performance parameters: [a] Power coefficients, C_P; [b]: Thrust coefficients, C_F. Performance curves are presented for shallow tip (H=0.15 m) and deep tip (H=0.44 m) immersions for a 20° hub pitch angle.

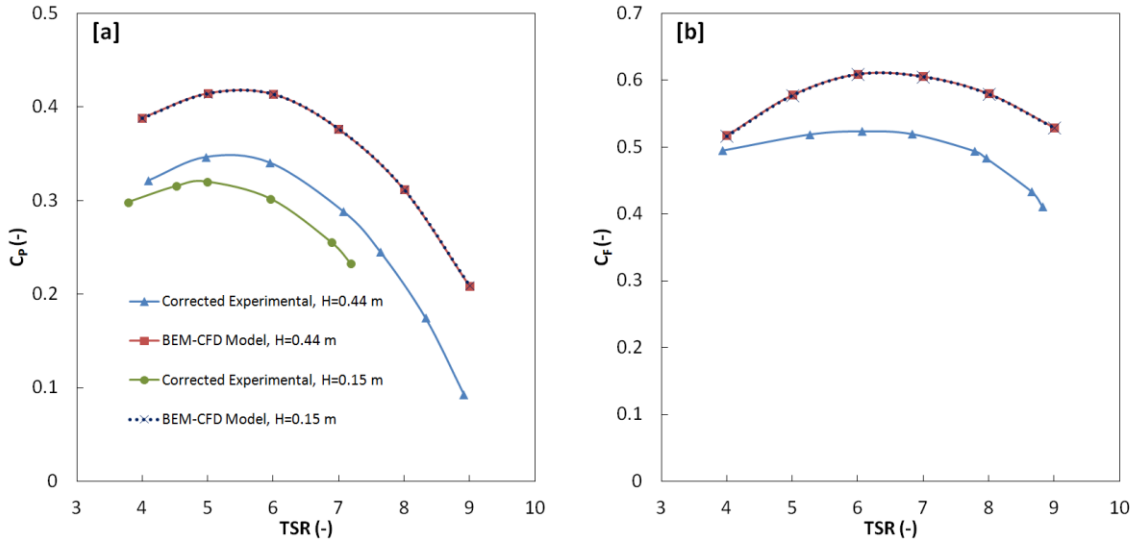

Figure 7 A comparison of experimental and BEM-CFD model performance parameters: [a] Power coefficients, C_P; [b]: Thrust coefficients, C_F. Performance curves are presented for shallow tip (H=0.15 m) and deep tip (H=0.44 m) immersions for a 25° hub pitch angle. Bahaj et al. [24] does not provide a thrust coefficient curve for the shallow tip immersion condition.

4.3 Blockage-Corrected Power and Thrust Coefficients

A reduction in blockage effects by increasing cross-sectional area within the computational model results in a reduction of power and thrust coefficient magnitudes (see Figure 8). This is due to the flow being allowed to expand more freely around the rotor causing less of the flow to pass through the rotor. Previously, it was shown that the difference between power coefficient curves predicted by the BEM-CFD model for the shallow and deep tip immersions was insignificant (see Figure 7). These findings indicate that the model is affected more significantly by blockage effects rather than the position of the rotor within the water column.

The reason why the power and thrust coefficient values predicted by the BEM-CFD model for the deep tip immersion case are significantly higher than the experimentally determined values is that Bahaj et al. [24] corrected their results for blockage. Their method was described earlier in Section 3.3 and aims to produce a more realistic value representative of the performance of the turbine for the flow conditions implemented but in the absence of the blockage which arises due to the confined cross-sectional area of the flume. The same methodology was applied to the BEM-CFD results, and by characterising downstream conditions based on velocities 15 diameter lengths from the rotor, power and thrust coefficients are much more consistent with the published experimental values (see Figure 8).

The blockage correction methodology implemented is very sensitive to the location of the downstream reference location, and a more appropriate method for determining the true performance attributes of a rotor is to place it in an unconstrained domain. This is more easily achieved numerically, and it is suggested based on the corresponding results that the correction method implemented by Bahaj et al. [24] over-compensates for blockage effects. At the peak performance TSR, the power coefficient for the

unconstrained domain is 3.88 % lower than that for the deep-tip immersion. Since power is a function of the cubic power of velocity, this is a reasonable estimate considering that the velocity at the rotor for the unconstrained domain was 1.11 % lower than the deep-tip immersion.

A further comparison is performed against the Classical BEM model presented in [7]. Agreement between the BEM and BEM-CFD model predictions of power coefficients improve at higher TSR values (see Figure 8a). With reduction of TSR, the BEM prediction tends closer towards the experimentally determined blockage-corrected values. There is strong agreement between predictions of thrust coefficients by the BEM and the CFD-BEM models (see Figure 8b).

Although the coupled BEM-CFD model is based on blade element momentum theory, there is a significant difference in the determination of blade forces in the two models. In the BEM model, there is no information regarding local flow speed and direction, and hence, the mean far field condition along a stream tube passing through the rotor is used. However, in the coupled model, velocities immediately upstream of the rotor are determined through the CFD model, where the flow is likely to contain some level of rotation. This means that the flow may impact the rotor at different angles which may not be parallel to the flow direction. This will affect the lift and drag forces exerted by the blade on the flow, and hence, the performance coefficients. As the CFD captures the influence of the rotor forces on the upstream flow, it is suggested that the BEM-CFD results are more representative of rotor performance in real flows.

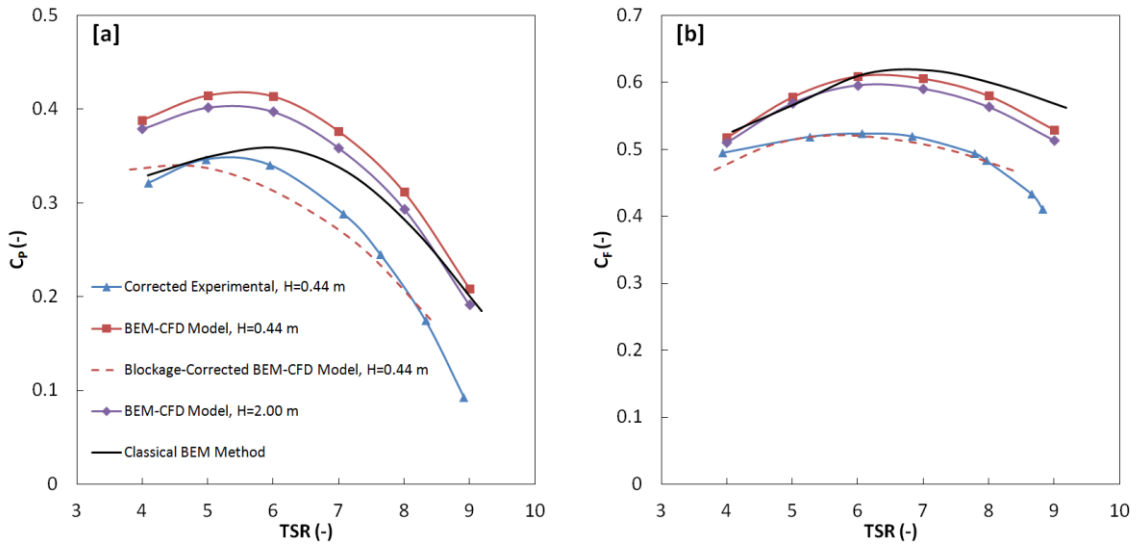

Figure 8 A comparison of experimental, BEM-CFD model and Classical BEM Method performance parameters: [a]: Power coefficients, C_P; [b]: Thrust coefficients, C_F. Performance curves are presented for deep tip immersions (H=0.44 m) and unconstrained conditions (H=2.0 m) for a 25° hub pitch angle.

4.4 The Impact of Immersion on Velocity Structure

The similarity between the performances of the shallow and deep tip immersion cases as determined from the BEM-CFD model can be linked to the hydrodynamics across each

rotor in the streamwise direction. This is illustrated by the velocity contours presented for a TSR of 6.0 and a hub pitch angle of 20° in Figure 9a and Figure 9b for shallow and deep tip immersions respectively.

For the shallow tip immersion, the close proximity of the water surface to the turbine appears to limit wake expansion along the top edge of the wake beyond approximately two diameters downstream. However, this does not appear to have any significant impact on the symmetry of the wake up to the water surface. Similarly, upstream of the turbine, the velocity contours also appear symmetrical up to the water surface. The low velocity regions downstream of the rotors are slightly longer for the deep tip immersion case, but again, the difference appears to be insignificant. Furthermore, the velocity magnitudes and structures immediately upstream and downstream are virtually identical for the two cases. Although the water surface results in a sudden cut-off of any vertical features in the flow, the knock-on effects of this on the underlying flow, including that at the elevation of the rotor, is not reflected in the predicted flow structure. This type of model is clearly only suitable where surface effects on flow around the rotor are negligible i.e. for a deep tip submersion.

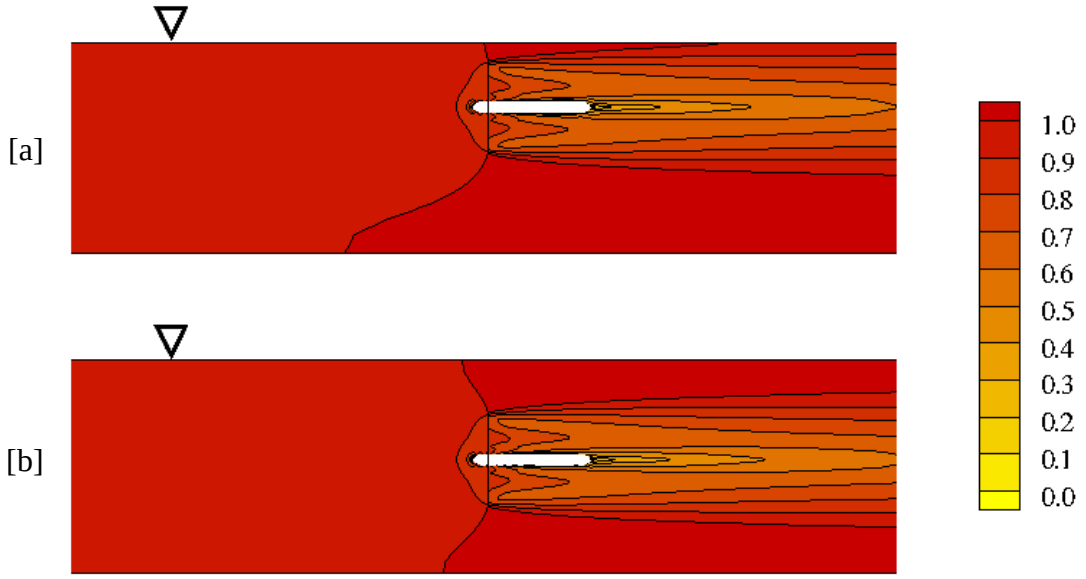

Figure 9 Normalised velocity contours on a lateral plane through the centre of a rotor for a tip speed ratio of 6.0 and a hub pitch angle of 25°. Plots are presented for [a]: shallow immersion (H = 0.15 m); [b]: deep immersion (H = 0.44 m). Velocities are normalised using the inlet velocity.

One reason for the similarity in performance is that, although the position of the rotor varies, the overall domain size is fixed for both cases. This ensures that the total flow rate through any plane normal to the axial direction is identical, although the distribution of velocity may be different. However, as the features of the rotor are time-averaged across the rotor disk any slight imbalance in velocity has a minimal effect on performance. Provided the rotor is not too close to one of the domain boundaries these results indicate that it is unlikely that the position of the rotor will have significant effect on performance in an enclosed domain.

Similarity in the flow structures around the turbines for the two immersion cases is also reflected in the streamlines passing through each rotor as shown in the horizontal plane in Figure 10a and Figure 10b for shallow and deep tip immersions respectively. Swirl within the downstream wakes is illustrated clearly by the streamlines. For the two cases, the high swirl regions occupy a similar cross-sectional area through the centre of the wake, and are very similar in magnitude, although this can be seen more clearly in Figure 10c where the variation in the normalised area mean angular velocity, $\bar{b}$, with distance downstream is shown for the two cases.

Velocity contours for the unconstrained domain in Figure 11 do not appear to be influenced by either the bottom or top boundary and the contours appear symmetrical along the centre of the rotor. Flow near the boundaries does not appear to be affected by the rotor and is equal in magnitude to the free-stream velocity which suggests that blockage effects are low. The low velocity region immediately downstream of the rotor is slightly longer than was previously observed for the shallow and deep tip immersion cases.

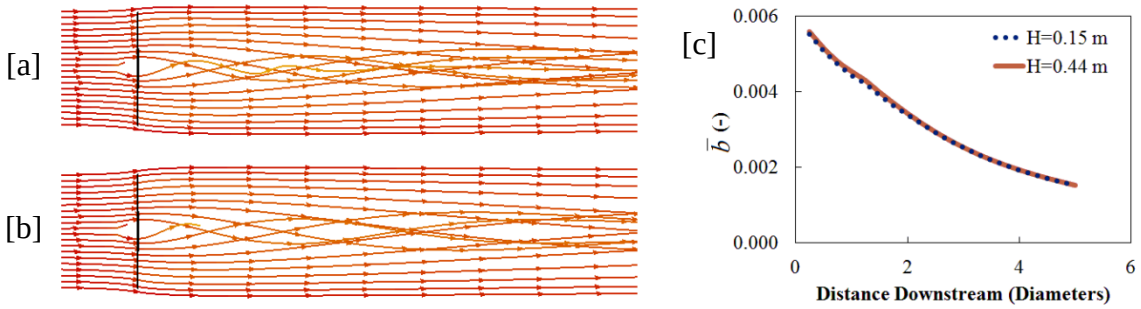

Figure 10 Lateral view of the streamlines passing through the rotor for a tip speed ratio of 6.0 and a hub pitch angle of 25° for [a]: shallow tip immersion (H=0.15 m); [b]: deep tip immersion (H=0.44 m). [c]: Magnitude of the normalised area mean angular velocity, $\bar{b}$, downstream of the two rotors.

Similarity in the velocity of the flow upstream of the rotors for the shallow and deep tip cases is further emphasised by the velocity profile along the centreline passing through the mid-radius of each rotor (see Figure 12a). Even for the unconstrained domain, the normalised velocity magnitude upstream of the rotor is similar to the other cases, although at the actual rotor, is in fact slightly lower by 0.93 % and 1.11 % when compared to the shallow and deep tip immersions respectively. The lower velocity may be linked to a lower blockage which would cause a greater proportion of the flow to be diverted away rather than being forced through the rotor. Further downstream of the rotor at a distance of 1.0 m and greater (see Figure 12a), velocities within the wake are significantly lower for the unconstrained domain indicating that wake development is affected significantly by the amount of blockage.

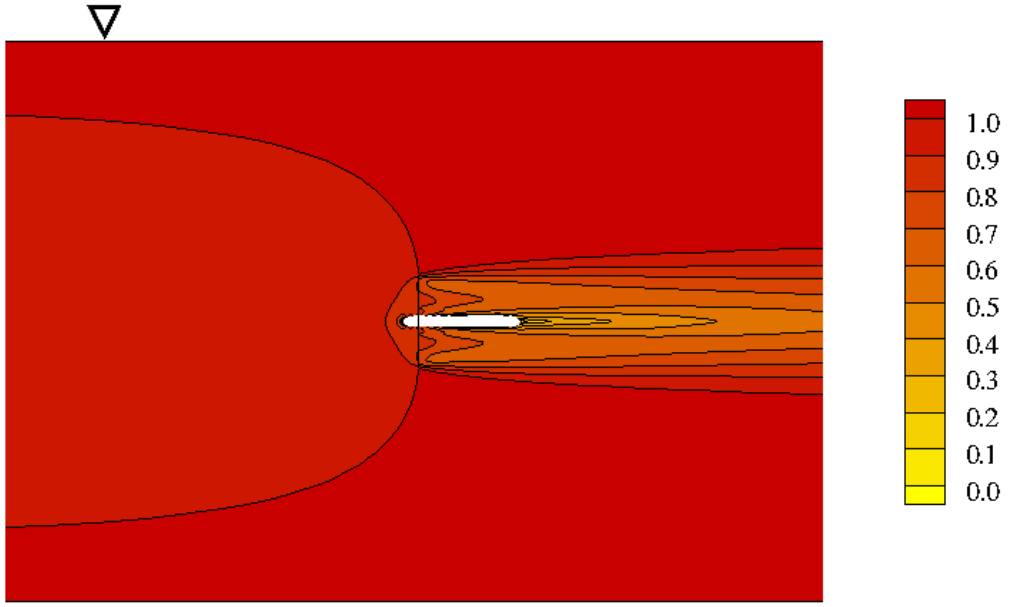

Figure 11 Normalised velocity contours on a lateral plane through the centre of a rotor for a tip speed ratio of 6.0, a hub pitch angle of 25° and an unconstrained domain (H = 2.0 m). Velocities are normalised using the inlet velocity.

Figure 12b shows the velocity profile across the height of the centre of the rotor disks. For the shallow and deep tip immersions, the only difference in velocity occurs towards the top of the rotor, where the normalised velocity for the shallow tip immersion case is 2.95 % higher than the corresponding value for the deep tip immersion case. This is evidence of the flow accelerating within the confined region between the top of the rotor and the water surface for the shallow immersion condition. There is very little difference between the velocities over the rest of the rotor. As for the unconfined domain, the normalised velocities across the rotor are consistently lower than the shallow and deep tip immersion cases, and by as much as 1.29 % when compared to the deep-tip immersion case.

4.5 The Impact of Immersion on Pressure Distribution

In reality the top of the water is a free-surface that will deform depending on motion of the flow within the tank. This free-surface effect is neglected in the computational model to significantly improve computational efficiency. However, this leads to blockage effects in the model, which in turn increases predictions of performance. The pressure contours in Figure 13 show an increase in pressure around the top of the rotor and the top of the domain for the shallow tip immersion case that is not present for the corresponding deep tip immersion domain. This indicates that if free-surface effects were included in the model there would be a larger displacement of the water in this region for the shallow tip immersion than the deep tip immersion domain. This would lead to less water being forced through the rotor, and lower efficiency for the shallow tip immersion case than the deep tip immersion case, and would correspond with the trends for the experiments.

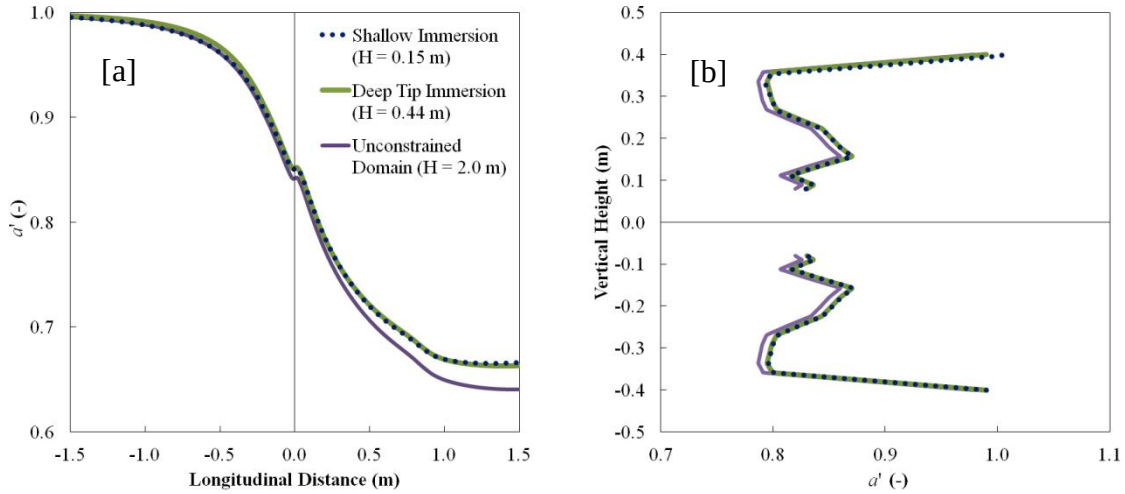

Figure 12 [a]: Profiles of normalised longitudinal velocities, *a*', at mid-radius through the rotor in the flow direction; [b]: Comparison of velocity profiles across the centre of the rotor disk in the vertical direction (-0.4 m ≤ y ≤ -0.08 m, 0.08 m ≤ y ≤ 0.4 m) for the shallow immersion, deep immersion and unconstrained conditions for a 25° hub pitch and a tip speed ratio of 6.0.

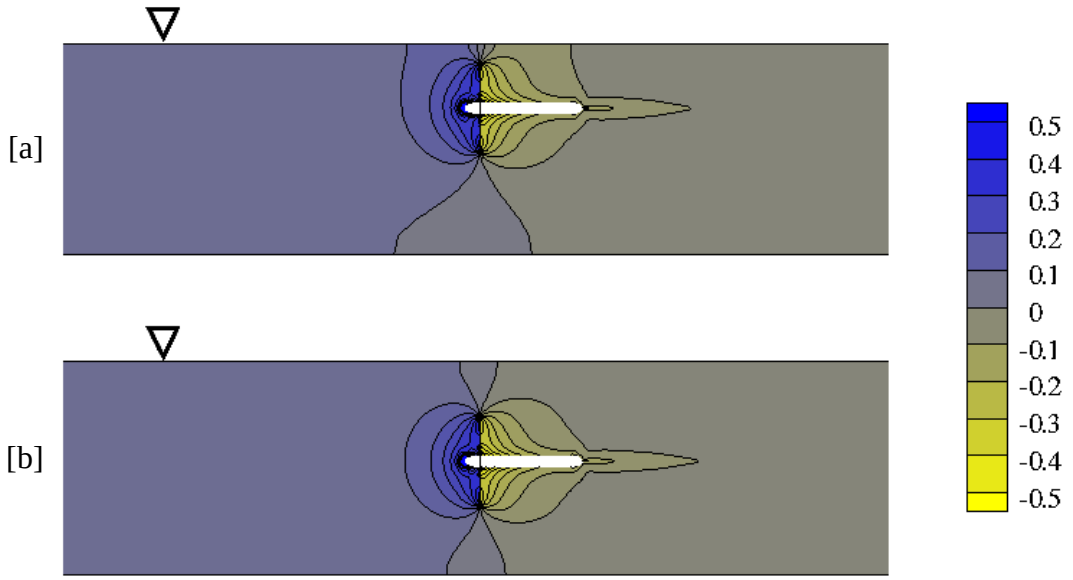

Figure 13 Normalised pressure contours on a lateral plane through the centre of a rotor for a tip speed ratio of 6.0 and a hub pitch angle of 25°. Plots are presented for [a]: shallow immersion (H = 0.15 m); [b]: deep immersion (H = 0.44 m). Pressures are normalised using the maximum value for each simulation.

5 Conclusions

The aim of this study was to present a practically useable tool that could be used in the context of tidal power to predict how tidal stream turbines may perform in typical offshore conditions. The model developed is based on the actuator disc principle which is

derived from blade element momentum theory: a modelling approach that is used extensively by the wind power industry.

Shorter run times and the relatively quick achievement of convergence can be attributed to the relative simplicity of the model when compared to the more sophisticated approach of explicitly modelling individual turbine blades. Due to a lower demand on computational resources, this model can be applied to considerably more complex engineering problems, particularly ones involving multiple devices arranged in arrays. This will be of particular use to developers and stakeholders requiring feasibility assessments based on net power outputs and for environmental impact assessments which are essential considering the high level of sensitivity associated with suitable offshore deployment sites. The model can also be used to predict the influence of tidal turbines on hydrodynamics, which can be used as guidance on how the positioning of downstream devices is likely to affect their performance.

Through the work presented, the significance of blockage effects and free-surface effects on rotor performance and wake development were identified. Blockage effects are easily avoided in a CFD approach by expanding the cross-sectional area of the model domain so as to avoid or minimise the artificial forcing of flow through the rotor. Free-surface effects are only significant in the upper part of the water column, and to meet the objective of developing an efficient low-demand model, the free-surface was not accounted for. The model can therefore only be used with confidence where free-surface effects are insignificant i.e. where a turbine is positioned deeper within the water column which is likely to be the case in offshore environments.

Given the requirement for a useable model, a very good match between the blockage-corrected BEM-CFD simulations and the published flume data was observed. Reliability of the model is further supported by good agreement with the classical BEM method which is widely used within the wind power industry, although variations in the C_P results are attributed to the BEM-CFD model's ability to account for the variation in velocity vectors of the flow upon impact with the rotor. It is therefore believed that the BEM-CFD model gives a more realistic estimation than the classical BEM method on turbine performance where the incoming flow is non-uniform due to interference by upstream devices, or due to complex natural bathymetries.

Due to the steady-state nature of the Reynolds-averaged simulations, and due to the time-averaged nature of the actuator disc approach, one of the key limitations of this model is its inability to capture transient features within the flow. This is likely to be significant, particularly within the immediate vicinity of the blades, and in the wake region immediately downstream of the rotor. However, several diameters downstream of the rotor, turbulence returns towards an isotropic state and its effects on the mean flow can be predicted more accurately by turbulent-viscosity models. Again, an unsteady solution would defeat the purpose of producing an efficient useable model, however, future work will address this uncertainty and explore methods of accounting for the influence of such transience at the rotor on the mean flow.

References

1. Willis, M., Masters, I., Thomas, S., Gallie, R., Loman, J., Cook, A., Ahmadian, R., Falconer, R., Lin, B., Gao, G., Cross, M., Croft, N., Williams, A., Muhasilovic, M.,

Horsfall, I., Fidler, R., Wooldridge, C., Fryett, I., Evans, P., O'Doherty, T., O'Doherty D. and Mason-Jones, A. 2010. *Tidal Turbine Deployment in the Bristol Channel - A Case Study*. Proceedings of the Institution of Civil Engineers - Energy. **163**(3): 93-105

2. Neil. S.P., Jordan, J.R. and Couch, S.J. 2012. *Impact of tidal energy converter (TEC) arrays on the dynamics of headland sand banks*. Renewable Energy. **37**: 387-397
3. O'Doherty, T., Egarr, D.A., Mason-Jones, A. and O'Doherty, D.M. 2009. *Assessment of axial loading on a 5 turbine array*. Proceedings of ICE, Energy. **162**(2): 54-65
4. Glauert, H. 1935. *Airplane propellers* in W.F. Durrand (ed) Aerodynamic Theory vol 4, Springer, 169-269.
5. Rajagopalan, R.G. and Mathur, S.R. 1993. *Three Dimensional Analysis of a Rotor in Forward Flight*. Journal of the American Helicopter Society. **38**(3): 14-25
6. Sørensen, J.N. and Kock, C.W. 1995. *A model for unsteady rotor aerodynamics*. Journal of Wind Engineering. **58**: 259-275
7. Masters, I., Chapman, J.C., Orme, J.A.C. and Willis, M.R. 2010. *A robust blade element momentum theory model for tidal stream turbines including tip and hub loss corrections*. Journal of Marine Engineering and Technology. **10**(1): 25-35
8. Hansen, M.O.L. 2008. *Aerodynamics of wind turbines*, 2nd edition, Earthscan, London.
9. Glauert, H. 1926. *The Elements of Aerofoil and Airscrew Theory*. Cambridge University Press.
10. Pitt, D.M. and Peters, D.A. 1981. *Theoretical prediction of dynamic-inflow derivatives*. Vertica. **5**(1): 21-34
11. Moriairty, P.J. and Hansen, A.C. 2005. *AeroDyn Theory Manual*. NREL
12. Shen, W.Z., Mikkelsen, R. and Sørensen, J.N. 2005. *Tip Loss Corrections for Wind Turbine Computations*. Wind Energy. **8**: 457-475
13. Buhl, M.L., Jr. 2004. *A New Empirical Relationship between Thrust Coefficient and Induction Factor for the Turbulent Windmill State.* NREL/TP-500-36834. Golden, CO: National Renewable Energy Laboratory, September.
14. Snel, H. 1998. *Review of the Present Status of Rotor Aerodynamics*. Wind Energy. **1**: 46-69
15. Crespo, A., Hernández, J. and Frandsen, S. 1999. *Survey of Modelling Methods for Wind Turbine Wakes and Wind Farms*. Wind Energy. **2**: 1-24
16. Leishman, J.G. 2002. *Challenges in Modelling the Unsteady Aerodynamics of Wind Turbines*. American Institute of Aeronautics and Astronautics Paper 2002-0037: 1-28
17. Snel, H. 2003. *Review of Aerodynamics of Wind Turbines*. Wind Energy. **6**: 203-211
18. Vermeer, L.J., Sørensen, J.N. and Crespo, A. 2003. *Wind turbine wake aerodynamics*. Progress in Aerospace Sciences. **39**: 467-510
19. Hansen, M.O.L., Sørensen, J.N., Voutsinas, S., Sørensen, N. and Madsen, H.A. 2006. *State of the art in wind turbine aerodynamics and aeroelasticity*. Progress in Aerospace Sciences. **42**: 285-330
20. Sanderse, B., van der Pijl, S.P. and Koren, B. 2011. *Review of CFD for wind-turbine wake aerodynamics*. Wind Energy. **14**(7): 799-819
21. Wu, T. Y. 1962. *Flow through a heavily loaded actuator disk*. Schiffstechnik. **9**: 47-134
22. *PHYSICA*, http://www.physica.co.uk

23. Croft, N., Pericleous, K. and Cross, M. 1995. *PHYSICA: A multiphysics environment for complex flow processes*. In: Taylor, C. et al. (eds) Numerical Methods in Laminar and Turbulent Flows Vol IX. Pineridge Press, Swansea.
24. Bahaj, A.S., Molland, A.F., Chaplin, J.R., Batten, W.M.J. 2006. *Power and thrust measurements of marine current turbines under various hydrodynamic flow conditions in a cavitation tunnel and towing tank.* Renewable Energy **32**: 407-426
25. Launder, B.E. and Spalding, D.B. 1972. *Mathematical models of turbulence*, Academic Press, London.
26. Batten, W.M.J., Bahaj, A.S., Molland, A.F., Chaplin, J.R. 2007. *Experimentally validated numerical method for the hydrodynamic design of horizontal axis tidal turbines*. Renewable Energy **32**: 2479-2490
27. Griffiths, R.T. and Woollard, M.G. 1978. *Performance of the Optimal Wind Turbine*. Applied Energy. **4**: 261-272
28. Versteeg, H.K. and Malalasekera, W. 2007. *An Introduction to Computational Fluid Dynamics: The Finite Volume Method.* 2nd edition, Pearson Prentice Hall, London.
29. Consul, C.A., Willden, R.H.J. and McIntosh, S.C. 2011. *An Investigation of the Influence of Free Surface Effects on the Hydrodynamic Performance of Marine Cross-Flow Turbines*. Proceedings of the European Wave and Tidal Energy Conference.
30. McBride, D., Croft, T.N. and Cross, M. 2008. *A coupled finite volume method for the computational modelling of mould filling in very complex geometries*. Computers & Fluids. **37**: 170-180